A cross-nearest neighbor/Monte Carlo algorithm for single-molecule localization microscopy defines interactions between p53, Mdm2, and MEG3

Nicholas C. Bauer[1] , Anli Yang[2,‡] , Xin Wang[2,‡], Yunli Zhou[2] , Anne Klibanski[2,§], and Roy J. Soberman[1,§,*]

From the [1]Division of Nephrology, Department of Medicine, Massachusetts General Hospital and Harvard Medical School, Charlestown, Massachusetts, United States; and [2]Neuroendocrine Unit, Department of Medicine, Massachusetts General Hospital and Harvard Medical School, Boston, Massachusetts, United States

Edited by Eric Fearon

The functions of long noncoding (lnc)RNAs, such as MEG3, are defined by their interactions with other RNAs and proteins. These interactions, in turn, are shaped by their subcellular localization and temporal context. Therefore, it is important to be able to analyze the relationships of lncRNAs while preserving cellular architecture. The ability of MEG3 to suppress cell proliferation led to its recognition as a tumor suppressor. MEG3 has been proposed to activate p53 by disrupting the interaction of p53 with mouse double minute 2 homolog (Mdm2). To test this mechanism in the native cellular context, we employed two-color direct stochastic optical reconstruction microscopy, a single-molecule localization microscopy technique, to detect and quantify the localizations of p53, Mdm2, and MEG3 in U2OS cells. We developed a new cross-nearest neighbor/Monte Carlo algorithm to quantify the association of these molecules. Proof of concept for our method was obtained by examining the association between FKBP1A and mTOR, MEG3 and p53, and Mdm2 and p53. In contrast to previous models, our data support a model in which MEG3 modulates p53 independently of the interaction with Mdm2.

Long noncoding RNAs (lncRNAs) function in cell-type and subcellular localization–dependent contexts; how they do so is incompletely understood. The human *MEG3* lncRNA gene is located on chromosome 14q32 and belongs to the conserved, imprinted *DLK1-MEG3* locus (1, 2). MEG3 transcripts are detected in a wide range of normal tissues, including endocrine tissues, brain, gonads, and placenta (1). MEG3 modulates the activity of multiple miRNAs; for example, MEG3 functions as a decoy for miR-138 (3) allowing it to regulate the generation of IL-1β in macrophages in models of host defense. MEG3 has also been reported to directly interact with DNA to modulate the transcription of TGF-β pathway genes (4).

Based on the observation that *MEG3* expression is lost in clinically nonfunctioning pituitary adenomas, we identified *MEG3* as a tumor suppressor (1, 5–7). Compared with normal tissue, MEG3 expression is also significantly reduced or absent in meningiomas (8), epithelial ovarian cancer (9), and squamous cell carcinoma of the tongue (10), supporting its role as a tumor suppressor. This function was further supported by studies of tumor xenograft growth in nude mice (11, 12). Several studies demonstrated that MEG3 expression causes an increase in cellular tumor antigen p53 (p53, UniProtKB P04637) levels and selectively activates p53 target gene expression (11, 13–16), suggesting that MEG3 exerts its cellular functions *via* p53. How the MEG3 lncRNA activates p53 remains unsolved.

p53 coordinates a transcription program to stall the cell cycle, promote DNA repair, and initiate senescence or apoptosis (17). The primary modulators of p53 activity are the E3 ubiquitin-protein ligase mouse double minute 2 homolog Mdm2 (Mdm2, UniProtKB Q00987) and its heterodimer partner protein Mdm4 (Mdm4, UniProtKB O1515) which constitutively polyubiquitinate p53 for proteasomal degradation, maintaining p53 at low levels (18–20). Thus, modulating the p53–Mdm2/4 interaction is a critical point of regulation for p53 activity. Signal-dependent posttranslational modification of p53, including phosphorylation and acetylation, can block Mdm2/4 from binding to p53 and prevent its degradation (21). Stabilization of p53 may also be achieved through interaction with other proteins such as peptidyl-prolyl cis-trans isomerase NIMA-interacting 1 (Pin1) (22, 23). It has been shown that MEG3 and p53 can be pulled down in one complex by immunoprecipitation (24, 25). Therefore, one possible mechanism for p53 activation by MEG3 is to disrupt the p53–Mdm2/4 interaction.

Identifying molecular associations within the spatial context of the cell is necessary to fully define the behavior of MEG3. Single-molecule localization microscopy (SMLM) is exceptionally well positioned to provide this information. SMLM is unique from other microscopy approaches in that it provides high-accuracy coordinates of the positions of fluorophores rather than an image (although an image may be reconstructed

from these localizations). As such, SMLM data must be analyzed with very different methods from traditional microscopy data which are still under active development (26). The first techniques applied traditional fluorescence image analysis approaches to the reconstructed images, although much of the unique information obtained by SMLM is lost this way. More promising approaches have looked at cluster-based and tessellation-based analyses (27, 28), enabling the examination of supramolecular assemblies. However, there has been little work done toward using SMLM data to measure single molecular interactions.

To fully understand the interactions of MEG3 with p53 and to test the hypothesis that MEG3 disrupts p53–Mdm2 binding, we developed a new cross-nearest neighbor/Monte Carlo algorithm to quantify the association between molecules from direct stochastic optical reconstruction microscopy (dSTORM) data. We characterized the behavior of this method *in silico* and demonstrated a proof of concept by examining the association between FKBP1A and mTOR, MEG3 and p53, and Mdm2 and p53. In contrast to previous models, our data support a model in which MEG3 modulates p53 independently of Mdm2. Future work will build on this technique to examine the relationships of MEG3 to other cell components.

Results

Quantifying macromolecular associations by SMLM

We developed an SMLM approach that allowed us to identify potentially interacting macromolecules by calculating the probability that two localizations were anomalously close. We applied a Monte Carlo estimation method (Fig. 1) that accounts for the local density around a candidate binding pair. This method is partly based on a technique recently introduced for examining the association of sparse mRNAs in neurons (29) but with substantial adaptations to deal with the unique properties of SMLM data.

In the first step, nearby localizations were grouped into "molecules" using spatial and temporal thresholds (Fig. 1, A and B). A characteristic of dSTORM is that there is no guarantee that a single molecule will be represented by a single localization. Consider the p53 tetramer; it may be bound by up to four primary single-epitope antibodies, each of which may be bound by one or two secondary antibodies, each of which may have zero to eight fluorophores attached (despite the average being ∼1 dye molecule/antibody), and each fluorophore may blink many times before permanent bleaching. A grouping algorithm is important for dSTORM data to remove such autocorrelated localizations for our downstream analysis, which here assumes that each molecule's location is independent of each other molecule.

Second, "molecules" from each channel were paired together through an exclusive cross-nearest neighbor algorithm: closest pair identified then removed, repeating until all possible pairs were made (Fig. 1, B and C). The resulting list of pairs is guaranteed to contain all detectable binding events.
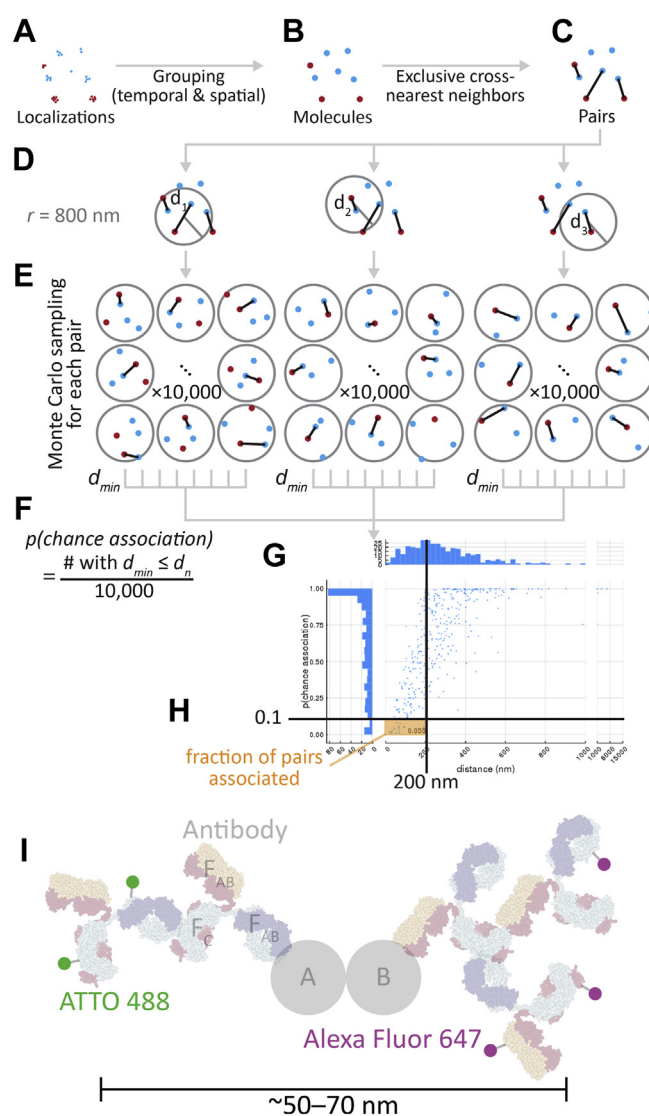

Figure 1. Cross-nearest neighbor/Monte Carlo method to estimate the fraction of molecules associated. Scattered localizations (*A*) were grouped over time and space to into "molecules" which have a position that is the average of their component localizations (*B*; see Fig. S5). These molecules were exclusively paired to their cross-nearest neighbors (*C*). For each pair (*D*), 10,000 permutations of the molecules within radius *r* (800 nm) of the centroid of the pair were generated, and the closest intermolecular distance was measured (*E*). The fraction of events less than the pair's distance was the probability of chance association (*p(chance association)*) (*F*). These values were accumulated across the whole cell (plotted in *G*), and the fraction of pairs with a probability of chance association <0.1 and within a physically possible binding distance (<200 nm), the fraction associated, was calculated (*H*). *I*, The physical arrangement of a bound pair and antibody stack. Typical immunofluorescence uses expensive, target-specific primary antibodies, and cheap secondary antibodies conjugated to a fluorophore like ATTO 488 and Alexa Fluor 647. For orientation, one antibody is labeled for its constant domain (F_C) and two antigen binding domains (F_{AB}). The physical size and arrangement mean that ∼50 to 70 nm may separate signal from the two fluorophores when detecting a binding interaction between proteins A and B, and multiple fluorophores can produce signal spread over tens of nanometers. Antibody graphic was created using NGL Viewer (56) from RCSB PDB 1IGT.

The third phase of the algorithm assesses the probability that each pair is associated by chance. Within the local neighborhood (radius *r* = 800 nm, Fig. 1*D*), 10,000 random permutations of the positions of the molecules within this

radius were generated, and the smallest paired distance is measured in each iteration (Fig. 1E). The fraction of permutations in which a distance d_n less than or equal to the observed distance d_{min} was recorded as the probability of chance association ($p(chance\ association)$) for that molecule pair (Fig. 1F). These steps were repeated for each pair in each cell, and a graph of distance and probability of chance association may be generated (Fig. 1G). This plot from a representative cell shows that larger distance is correlated with higher probability of chance association, with wide variability because of local density changes.

Finally, these pairwise measures of association were reduced into a summary value which would correlate with fraction

bound. We considered pairs with a probability of chance association less than 0.1 and a distance of less than 200 nm to be associated and used that value to generate the final output, fraction associated (Fig. 1H). In this example, the average distance of the pairs in the associated fraction is approximately 50 nm, which corresponds well with the range expected because of the size of the antibody stacks used to detect molecules (up to ~50–70 nm between fluorophores, Fig. 1I). The largest expected distances would come from the p53 tetramer, which would potentially add another 5 to 10 nm to the distance between fluorophores but well within the 200 nm cutoff chosen. In this dataset, pairs with a large distance but a low probability of chance association were rare; most of those
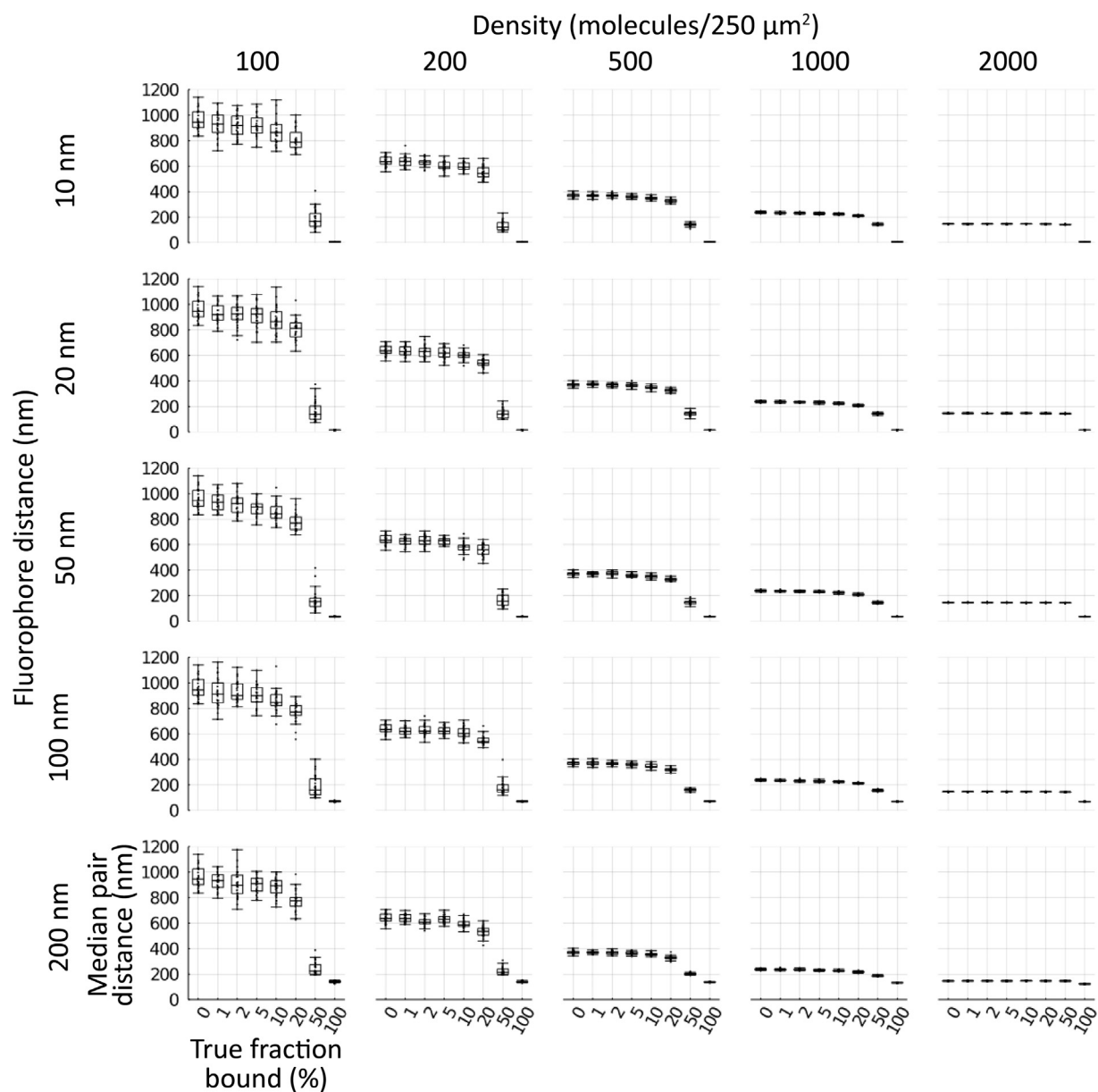

Figure 2. Density and pair distance determine median distance. Simulated cells of 100, 200, 500, 1000, and 2000 molecules of each type (columns *left* to *right*) within a 250 µm² circle with 10, 20, 50, 100, and 200 nm separation between pairs (rows *top* to *bottom*) for cells with 0, 1, 2, 5, 10, 20, 50, or 100% binding were generated (n = 30 each condition). Molecules for each simulated cell were run through the cross-nearest neighbor/Monte Carlo algorithm and median distance between pairs measured. *Boxes* indicate median ± upper and lower quartile; *whiskers* indicate the range excluding outliers.

pairs classified as unassociated were because of moderately close pairs in dense areas.

Algorithm performance improves with lower density, shorter distances

A natural limitation of this algorithm is that it strongly depends on the density of localizations and the distance between the fluorophores of an associated pair. To characterize this behavior, we simulated 30 distributions of molecules (*i.e.*, the product of the grouping algorithm described above) for each combination of density (100, 200, 500, 1000, 2000, 5000, and 10,000 molecules of each kind within a 250 μm² circle),

percent binding (0, 1, 2, 5, 10, 20, 50, and 100%), and physical distance between fluorophores (10, 20, 50, 100, and 200 nm). Higher density naturally means that the two sets of localizations are closer together on average (Fig. 2, columns from left to right), while larger binding distance inflates the value they converge to as more of the molecules are bound together (Fig. 2, rows from top to bottom). The Monte Carlo component of the association algorithm adjusts for local density around a putative associated pair, but the algorithm's sensitivity is reduced by higher global density (Fig. 3, columns from left to right). Larger physical distance between fluorophores in a bound pair similarly reduces sensitivity, as the pair becomes
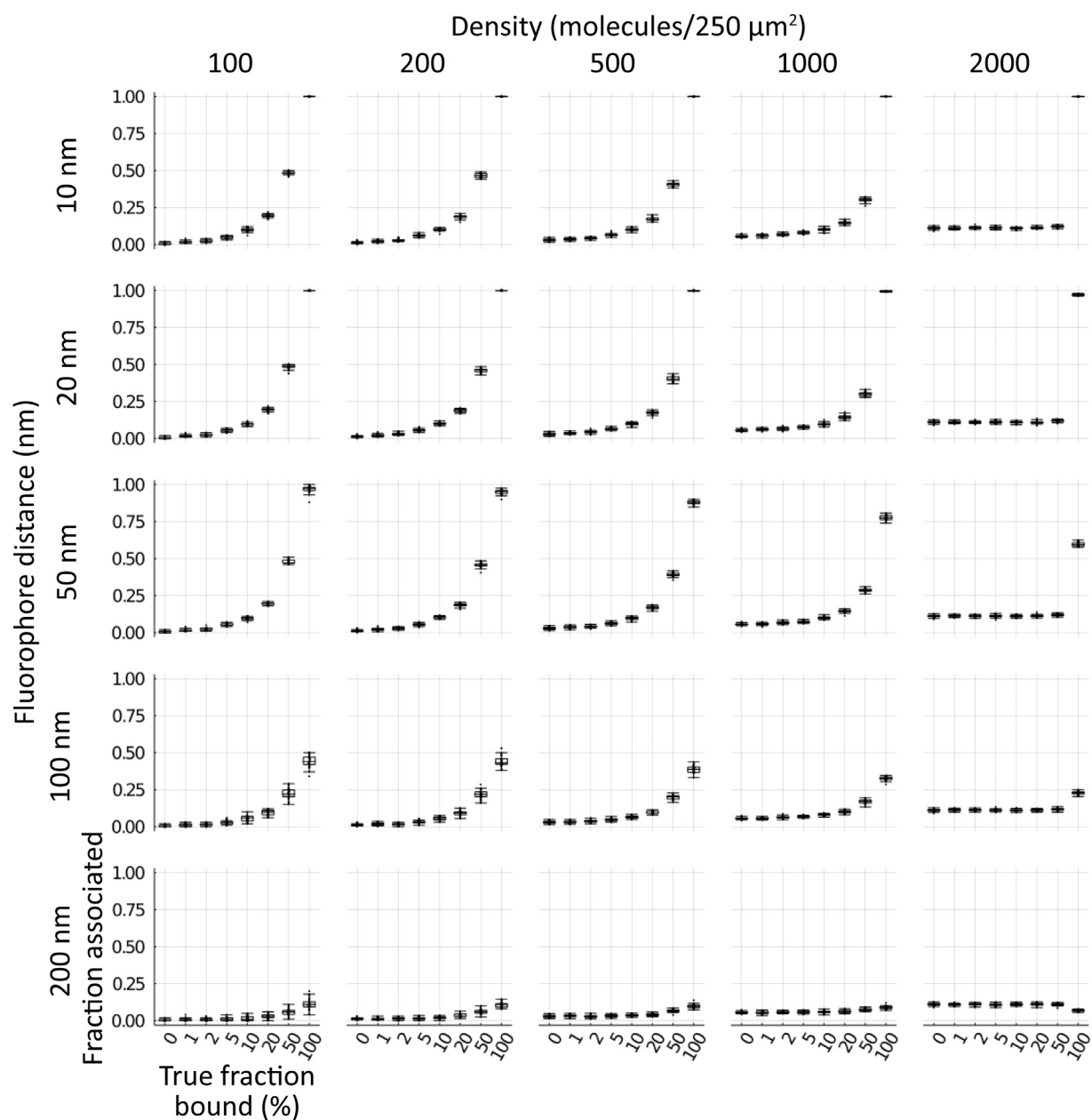

Figure 3. Density and pair distance influence fraction associated. Simulated cells of 100, 200, 500, 1000, and 2000 molecules of each type (columns *left* to *right*) within a 250 μm² circle with 10, 20, 50, 100, and 200 nm separation between pairs (rows *top* to *bottom*) for cells with 0, 1, 2, 5, 10, 20, 50, or 100% binding were generated (n = 30 each condition). Molecules for each simulated cell were run through the cross-nearest neighbor/Monte Carlo algorithm and median distance between pairs measured. Boxes indicate median ± upper and lower quartile; *whiskers* indicate the range excluding outliers.

harder to distinguish from the background distribution (Fig. 3, rows from top to bottom). Normalizing the fraction associated using 0% and 100% mean values improves the correspondence between true fraction bound and measured fraction associated, but the measured value becomes a severe underestimate of the true fraction bound at higher densities and increased pair distances and can produce hard to interpret negative values (Figs. S1 and S2). We chose not to apply this simulated normalization approach to the biological data, though a similar approach could be useful in an advanced iteration of our method.

Detection of FKBP1A–mTOR interaction

To characterize the algorithm in a known biological system, we chose to look at the well-characterized rapamycin-induced binding of peptidyl-prolyl cis-trans isomerase FKBP1A (FKBP1A, UniProtKB P62942) and serine/threonine kinase mTOR (mTOR, UniProtKB P42345) (30). U2OS osteosarcoma cells were treated with 0 or 10 ng/ml rapamycin for 24 h and then fixed. FKBP1A was labeled with a secondary antibody conjugated with Alexa Fluor 647 (magenta), and mTOR was labeled with a secondary antibody conjugated to ATTO 488 (green). Large tiled widefield fluorescence images were taken (Fig. S3), and 10 individual cells were randomly selected from these fields for dSTORM analysis, in each of five replicates (Fig. S4). Representative cells are shown in Figure 4A, widefield (left three columns) and dSTORM localizations and grouped molecules (right two columns, respectively). Expected strong nuclear mTOR fluorescence and cytoplasmic FKBP1A fluorescence is apparent, with no large-scale change upon rapamycin treatment. As seen in the detail of the molecule groups (right column), the grouping operation is slightly biased toward merging nearby clusters.

Using our cross–nearest neighbor/Monte Carlo method, we were able to detect a strong, significant increase in fraction associated of FKBP1A–mTOR pairs with rapamycin treatment, from 0.0749 ± 0.02504 to 0.121 ± 0.0286, by ANOVA with rapamycin treatment within replicates (F = 11.83, p = 0.02630, ω^2 = 0.2687) (Fig. 4). The 0 ng/ml data make clear that the method does not measure direct binding but association; factors other than binding interactions can lead to associations between molecules. Instead, we suggest the data produced by this method be interpreted as measuring relative differences in association, and that data from a single condition are probably insufficient independent evidence to determine if two molecules are associated. The strength of rapamycin-induced binding leads to the question of why the fraction association with rapamycin present is not higher. The fraction of pairs of detected molecules may not represent the total number of pairs available for binding. Pair members may be held apart by compartmentalization or binding may be blocked by other factors. With this interaction, mTOR is present in two separate complexes, mTOR complex 1 and 2 (MTORC1/2); MTORC1, but not MTORC2, may be bound by FKBP1A because of steric hindrance caused by other components in MTORC2 (30). Also as noted in the previous section,

dense labeling and lengthy distances between fluorophores may also lead to underdetection of true associations.

For comparison, we also applied a naïve median distance approach, where we calculated the median of the pairwise distances for each cell (Fig. 4). In this simple approach, there was a high degree of overlap between conditions and a significant but moderate decrease in median distance, from 380 ± 106.3 nm to 337 ± 83.4 nm (F = 15.97, p = 0.01618, ω^2 = 0.04774) (Fig. 4). Thus, our cross-nearest neighbor/Monte Carlo–based approach provides a stronger and more robust measure of association over simpler approaches.

MEG3 associates with p53 and is insensitive to MEG3 induction

We developed U2OS osteosarcoma cell clones containing a doxycycline-inducible MEG3 (U2OS-MEG3) and confirmed that MEG3 was induced 100 to 200-fold on doxycycline treatment as determined by qRT-PCR. We established conditions for performing dSTORM, simultaneously imaging RNA using fluorescence *in situ* hybridization (FISH) and proteins by immunofluorescence. After 20 h induction with doxycycline, cells were fixed and MEG3 was labeled with a tiled probe set conjugated with Quasar 670 (magenta), and p53 was labeled with a secondary antibody conjugated to ATTO 488 (green). Cells were separately labeled for *GAPDH* mRNA with a tiled probe set conjugated with Quasar 570 (magenta) as a negative control. Large tiled widefield fluorescence images were taken (Fig. S5), and 10 individual cells were randomly selected from these fields for dSTORM, in each of three replicates (Fig. S6). Representative cells are shown in Figure 5, widefield (left three columns) and dSTORM localizations and grouped molecules (right two columns, respectively). The intense fluorescence indicating MEG3 is readily apparent in the nucleus of the cells treated with doxycycline, along with p53, while very little MEG3 is apparent in untreated cells (Fig. 5A). Doxycycline treatment had no apparent effect on the GAPDH mRNA distribution (Fig. 5B).

Using our cross-nearest neighbor/Monte Carlo method, we found a stark difference between MEG3 and *GAPDH* mRNA in terms of fraction associated (Fig. 6A). ANOVA of doxycycline treatment within replicates and between RNAs demonstrated that the fraction associated was significantly larger for MEG3 than for *GAPDH* mRNA (F = 14.41, p = 0.01917, ω^2 = 0.3497). Because only the RNA main effect was significant, a follow-up one-way ANOVA was performed within each RNA type. For *GAPDH* mRNA, no change due to doxycycline was observed (-Dox (white box): 0.0430 ± 0.00312 versus +Dox (gray box): 0.0422 ± 0.00770; F = 0.04628, p = 0.8496, ω^2 = -0.03593) (Fig. 6A, right). There are several reasons why the method may detect a very low level of association between p53 and *GAPDH* mRNA. Some level of background associations may be expected because of density of localizations. p53 is also known to have promiscuous nonspecific RNA binding capacity (31). Another contributor may be crosstalk because of the spectral overlap of the fluorophore used for *GAPDH* mRNA and p53 (Quasar 570 versus ATTO 488). However, we expect
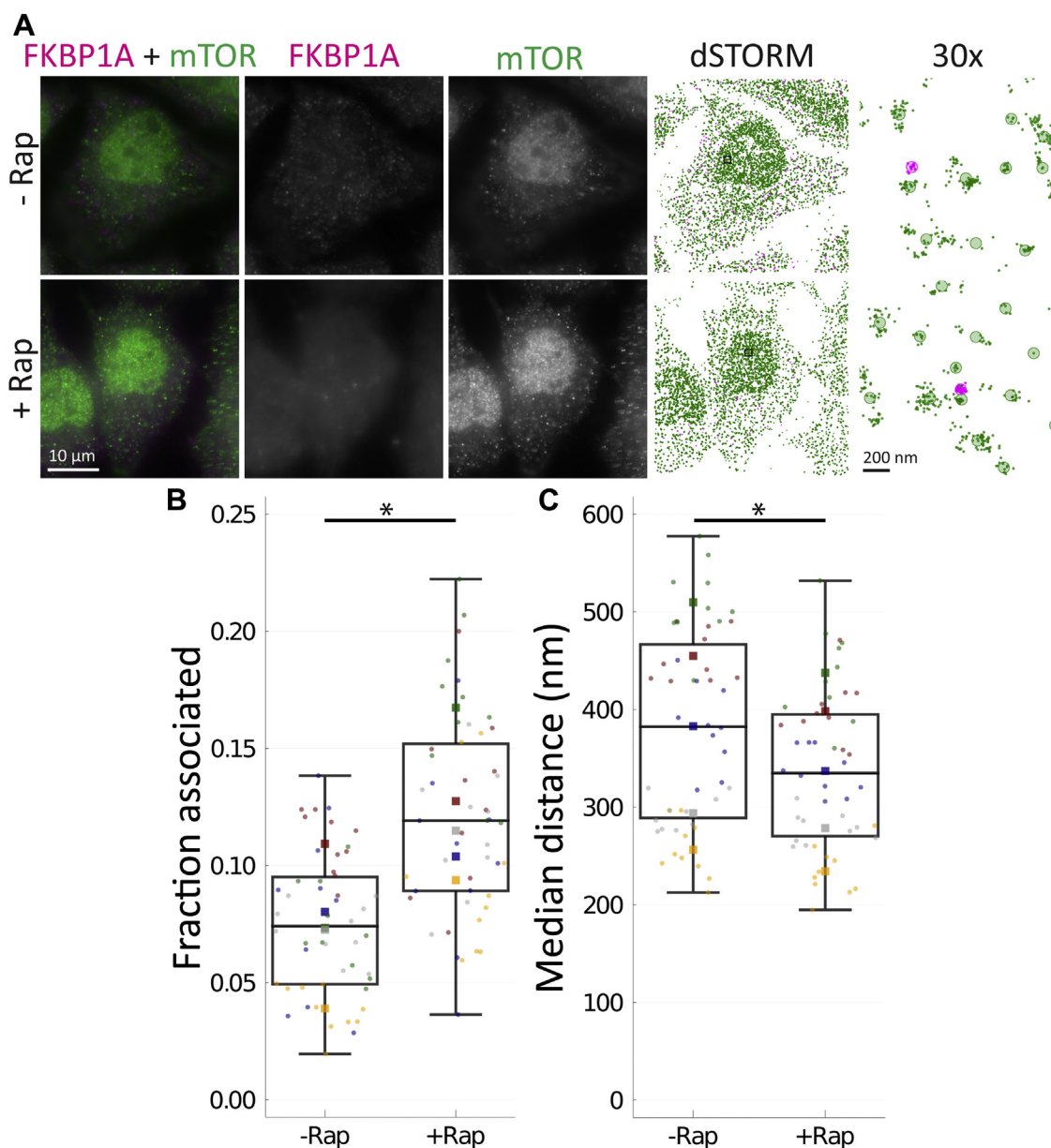
Figure 4. Method detects rapamycin-induced FKBP1A association with mTOR. U2OS-MEG3 cells were treated for 24 h with or without 10 ng/ml rapamycin. *A*, cells were stained for mTOR with a secondary antibody conjugated to ATTO 488 (*green*) and for FKBP1A with a secondary antibody conjugated to Alexa Fluor 647 (*magenta*). From *left* to *right*: Merged image; RNA channel; p53 channel; dSTORM localization map; 30x inset of dSTORM localizations in the *black box*, with *shaded circles* indicating "molecules". Scale bars are 10 μm, or 200 nm (*right column*). *B*, fraction of pairs associated, as defined by a probability of chance association <0.1 (*i.e.,* correction for local density) and distance <200 nm (upper limit for binding distance, accounting for error). *C*, median distance between pairs for each cell (nm). *Boxes* indicate median ± upper and lower quartile; *whiskers* indicate the range excluding outliers. Data points are colored by replicate. For each condition, single molecule localizations were collected from 10 randomly chosen cells in five separate experiments. Means for each replicate are indicated by same-colored squares. * indicates $p < 0.05$ by ANOVA. dSTORM, direct stochastic optical reconstruction microscopy.

true molecular associations to lead to a much higher measured fraction associated.

In contrast with *GAPDH* mRNA, the fraction of MEG3 associated with p53 was substantially higher than with *GAPDH* mRNA, and doxycycline induction had a medium-large effect but was not significantly different (-Dox (white box): 0.103 ± 0.0149, +Dox (gray box): 0.0700 ± 0.02888; F = 5.136, p = 0.1516, ω^2 = 0.1212) (Fig. 6*A*, left). A reduction or no change in fraction of MEG3 associated with p53 following MEG3 induction suggests that MEG3 binding to p53 stays roughly

constant as the level of MEG3 increases. Because the fraction is based on the number of pairs and MEG3 is the limiting factor, little change in fraction bound when MEG3 expression is induced implies a substantial increase in the absolute number of associations between MEG3 and p53 in the cell. MEG3 also interacts with numerous other macromolecules, including polycomb repressive complex 2 (PRC2) (32, 33), which may absorb much of the increased levels of MEG3.

For comparison, we also applied a naïve median distance approach, where we calculated the median of the pairwise
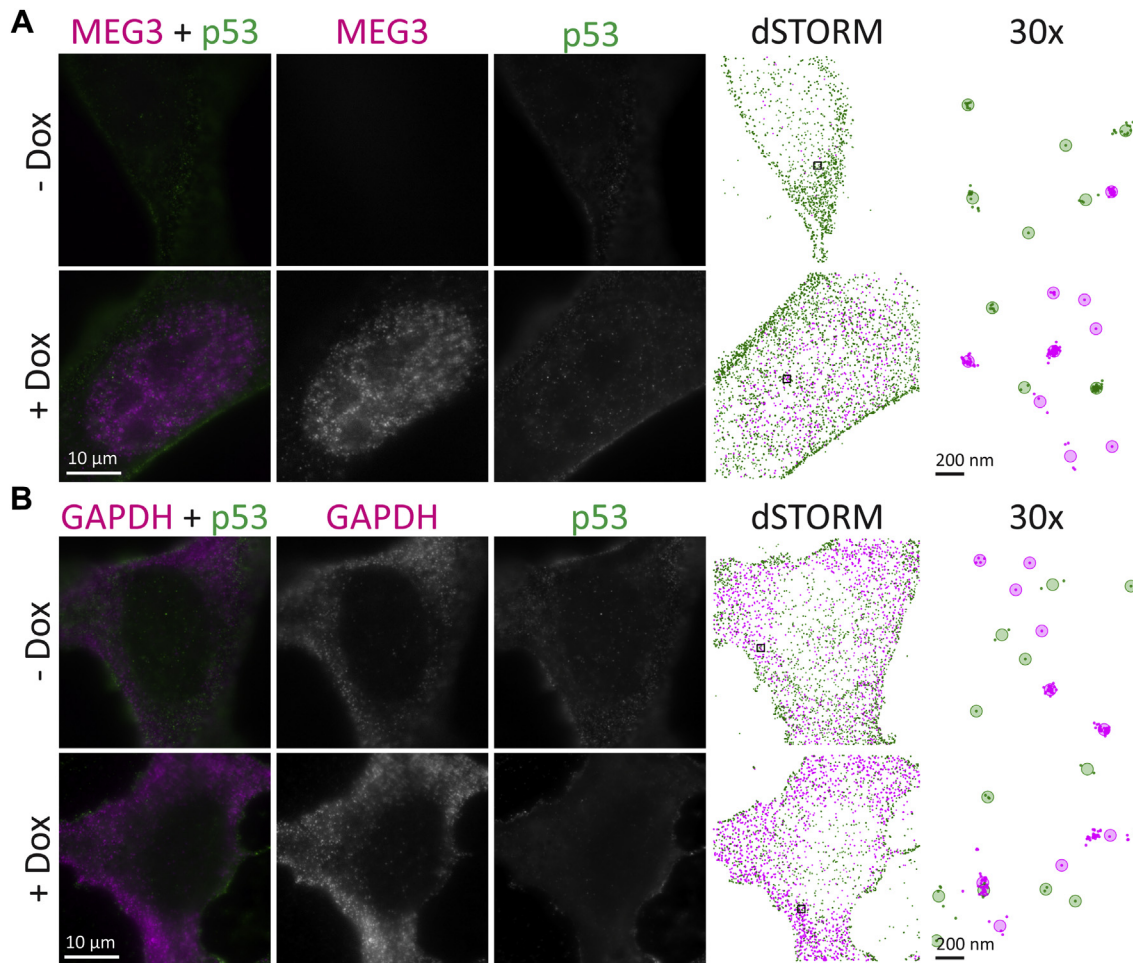
Figure 5. MEG3 localized in the nucleus of U2OS cells by epifluorescence and 2-color dSTORM. *MEG3* was induced by treatment of U2OS-MEG3 cells for 20 h with 1 μg/ml doxycycline. Cells were stained for p53 with a secondary antibody conjugated to ATTO 488 (*green*) and either tiled oligonucleotides recognizing MEG3 (Quasar 670, *magenta*, *A*) or GAPDH (Quasar 570, *magenta*, *B*). From *left* to *right*: Merged image; RNA channel; p53 channel; dSTORM localization map; 30x *inset* of dSTORM localizations in the *black box*, with *shaded circles* indicating "molecules". Scale bars are 10 μm, or 200 nm (right column). dSTORM, direct stochastic optical reconstruction microscopy.

distances for each cell (Fig. 6*B*). In this simple approach, there was a high degree of overlap between MEG3 and *GAPDH* mRNA distributions, and no overall effect of RNA on median distance was found (487 ± 151.8 nm to 420 ± 105.0 nm; F = 0.2344, *p* = 0.6535, ω^2 = -0.05747) (Fig. 6*B*). These data support our cross-nearest neighbor/Monte Carlo–based approach as providing a more consistent and robust measure of association over simpler approaches.

Mdm2–p53 binding maintains stable equilibrium

To determine whether MEG3 causes accumulation of p53 by disrupting the Mdm2–p53 interaction, MEG3 was induced by doxycycline in U2OS-MEG3 cells, with or without the addition of the Mdm2–p53 binding inhibitor nutlin-3a. After 24 h of treatment, the cells were fixed. p53 was labeled with a secondary antibody conjugated to Alexa Fluor 647 (magenta), and Mdm2 was labeled with a secondary antibody conjugated to ATTO 488 (green). Large tiled widefield fluorescence images were taken (Fig. S7), and 10 individual cells were randomly selected from these fields for dSTORM analysis, in each of three replicates (Fig. S8). Representative cells are

shown in Figure 7, widefield (left three columns) and dSTORM localizations and grouped molecules (right two columns, respectively). Intense nuclear p53 fluorescence is observed on treatment with nutlin-3a, without much apparent change due to doxycycline. Mdm2 levels and localization change little between conditions.

Using our cross-nearest neighbor/Monte Carlo method, we found that nutlin-3a treatment caused a large but not significantly different change in p53–Mdm2 association by ANOVA with nutlin-3a and doxycycline within replicates (-Nut: 0.0727 ± 0.01209, +Nut: 0.0517 ± 0.01703; F = 10.76, *p* = 0.08174, ω^2 = 0.1289) (Fig. 8*A*). Doxycycline treatment (MEG3 induction) had a small but not significantly different change (-Dox: 0.0565 ± 0.01230, +Dox: 0.0680 ± 0.02169; F = 3.265, *p* = 0.2125, ω^2 = 0.02983). There was no significant interaction effect (F = 0.1912, *p* = 0.7046, ω^2 = -0.05837). Importantly, these data suggest that MEG3 does not disrupt the overall level of p53–Mdm2 binding. However, nutlin-3a also did not definitively disrupt p53–Mdm2 binding by this measure. These observations may in part be explained through equilibrium. For example, nutlin-3a inserts into the pocket of Mdm2 that
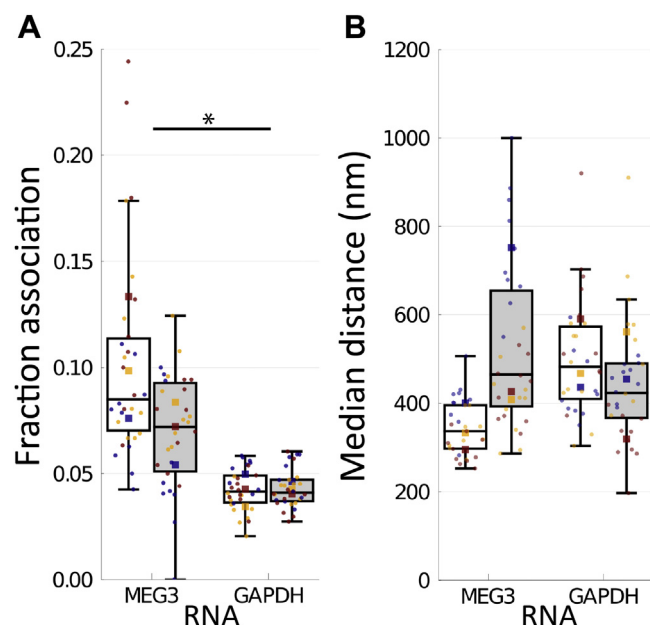
Figure 6. MEG3 associated with p53. *MEG3* was induced by treatment of U2OS-MEG3 cells for 20 h with (*gray*) or without (*white*) 1 μg/ml doxycycline. The cells were then fixed and stained for 2-color dSTORM of MEG3 and p53 (*left*) or *GAPDH* mRNA and p53 (*right*). For each condition, single molecule localizations were collected from 10 randomly chosen cells in three separate experiments. *A*, fraction of pairs associated, as defined by a probability of chance association <0.1 (*i.e.,* correction for local density) and distance <200 nm (upper limit for binding distance, accounting for error). *B*, median distance between pairs for each cell (nm). *Boxes* indicate median ± upper and lower quartile; *whiskers* indicate the range excluding outliers. Data points are colored by replicate. Means for each replicate are indicated by same-colored *squares*. * indicates *p* < 0.05 by ANOVA. dSTORM, direct stochastic optical reconstruction microscopy.

binds to p53, preventing Mdm2 from ubiquitinating p53 and marking it for proteasomal destruction (34). Thus, levels of both proteins may accumulate until they reach a high enough concentration to overcome the effect of nutlin-3a. It is also possible that the effects of nutlin-3a are more nuanced. Nutlin-3a has been shown to block Mdm2-mediated poly-ubiquitination and transrepression of p53 (35, 36), and nutlin-3a causes Mdm2 to rapidly deplete from an artificial concentration of p53 (37) but does not block monoubiquitination, and complexes were still observed by proximity ligation assay (36). These studies suggest that nutlin-3a may reduce high-affinity binding but not strongly affect transient interactions. Our results are consistent with this model.

For comparison, we again conducted an analysis based on naïve median distances. As with MEG3–p53 binding, we found this simple approach produced overlapping distributions and less interpretable results. Nutlin-3a was associated with a large but not significant decrease in median distance (-Nut: 273 ± 36.2 nm, +Nut: 224 ± 38.2 nm; F = 11.60, *p* = 0.07643, ω^2 = 0.2049) (Fig. 8*B*). Doxycycline was not associated with any change in median distance (-Dox: 250 ± 34.6 nm, +Dox: 247 ± 55.2 nm; F = 0.02689, *p* = 0.8848, ω^2 = -0.02940), and there was a small but nonsignificant interaction effect (F = 1.271, *p* = 0.3767, ω^2 = 0.01809). The decrease in distance due to nutlin-3a is likely because of the increase in p53 expression levels when Mdm2 is inhibited from marking p53 for degradation.

Discussion

We developed a mathematical approach for analyzing SMLM data that we used to interrogate the interactions of MEG3. Our overall approach takes advantage of high-resolution molecule position data to calculate distances between putative binding partners, assesses the probability that the two molecules are not associated, and thus provides an overall measure of the fraction of pairs of molecules likely associated. Using this technique, we distinguished between nonbinding pairs (*GAPDH* mRNA–p53) and binding pairs (MEG3–p53, FKBP12–mTOR) inside cells and quantified the extent of association between Mdm2 and p53. The mechanism of MEG3 action suggested by our experiments is different than the previously proposed mechanism in which MEG3 acts by protecting p53 from polyubiquitination by Mdm2. Moreover, the fraction of association assessed between MEG3 and p53 indicates that there are insufficient stable interactions occurring to directly compete against p53–Mdm2 binding. These data suggest that MEG3 activates p53 through alternative mechanisms.

Under MEG3 induction, p53 transcription activation is selective, inducing certain p53 targets (*e.g., GDF15*) but failing to induce other p53 targets (e.g., *CDKN1A*) (16). A MEG3–p53 complex may not be competent to induce Mdm2 expression, thereby suppressing the negative feedback regulatory loop. MEG3 also interacts with the chromatin remodeler PRC2 (32, 33), which is responsible for forming heterochromatin at target sites. MEG3 targets PRC2 to certain sites *via* DNA triplex formation (*e.g.,* TGF-β pathway genes) (4) and protects other sites from PRC2 activity (*e.g., MEG3* locus) (38). A recent investigation of MEG3 structure identified a pseudoknot in MEG3 critical for MEG3-dependent p53 activation, which however was not directly involved in p53 binding (39). It is also possible that MEG3 may modulate the activity or binding affinity of Mdm2 on p53 by forming a ternary complex with them. Similar interactions have been observed with p14[ARF] (tumor suppressor ARF) (40), UCH-L1 (ubiquitin carboxyl-terminal hydrolase isozyme L1) (41), and the 5S RNP (42). Future work will need to address these alternative mechanisms. This algorithm could be expanded to consider ternary interactions to investigate these pathways.

There are some important challenges to the cellular SMLM-based association analysis we have developed and which affect SMLM analysis approaches in general. First, despite the 10 to 20 nm resolution of each localization, the large distance between the molecule of interest and the fluorophore limits the analytical resolution. A typical two-antibody stack can have a displacement of up to ∼35 nm from the bound epitope to the conjugated fluorophore; thus, the fluorophores for a bound pair of molecules may be separated by ∼50 to 70 nm or more (Fig. 1*I*), depending on the distance between epitopes. In addition, the antibody stack may be free to rotate and flex at the neck, adding variability in the position of the fluorophore during imaging (43). High density also impacts ability to differentiate low fraction associated, as illustrated in Figure 3. These distance issues may be addressed in part using
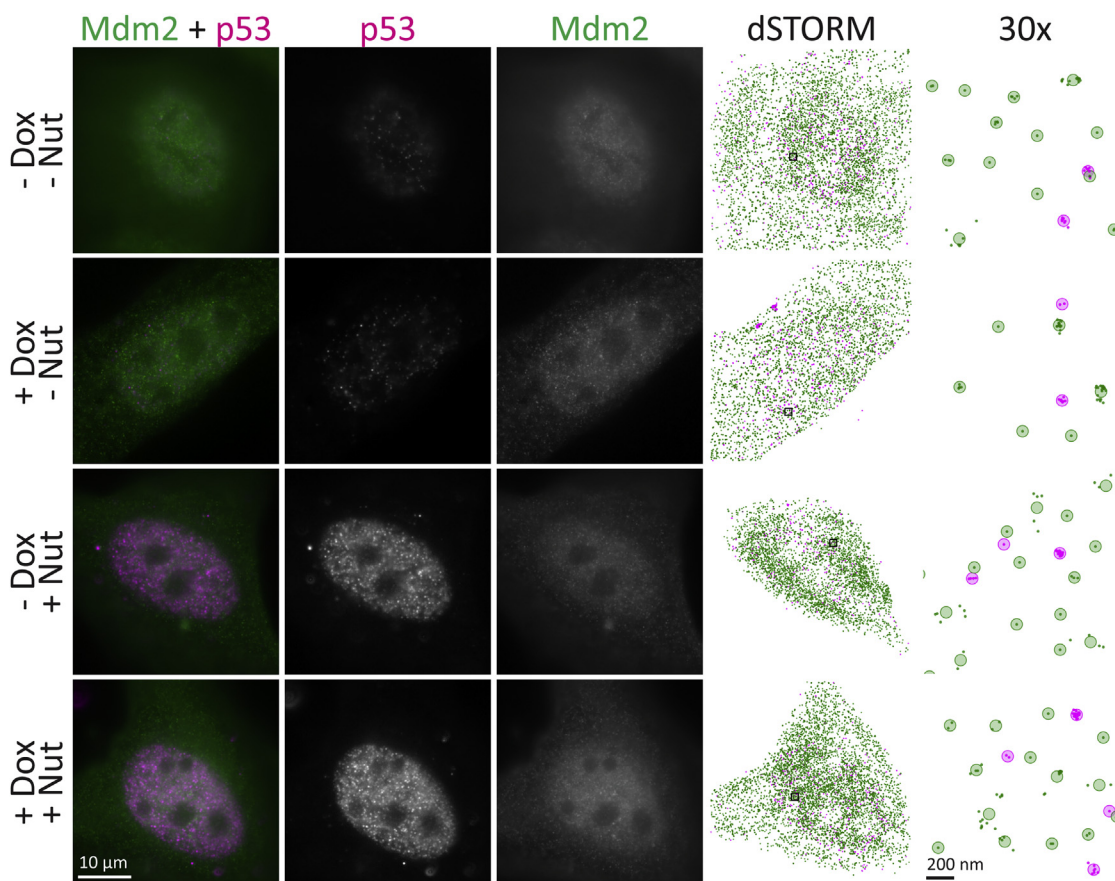
Figure 7. Nutlin-3a caused accumulation of p53 in the nucleus. *MEG3* was induced by treatment of U2OS-MEG3 cells for 20 h with 1 μg/ml doxycycline and/or 10 μM nutlin-3a. Cells were stained for Mdm2 with a secondary antibody conjugated to ATTO 488 (*green*) and for p53 with a secondary antibody conjugated to Alexa Fluor 647 (*magenta*). From *left* to *right*: Merged image; RNA channel; p53 channel; dSTORM localization map; 30x inset of dSTORM localizations in the *black box*, with *shaded circles* indicating "molecules". Scale bars are 10 μm or 200 nm (right column). dSTORM, direct stochastic optical reconstruction microscopy.

nanobodies as secondary antibodies, which would reduce the distance to ∼30 to 50 nm (Fig. 9*A*). Nanobodies are small single-domain antibody fragments derived from camelids that are emerging as powerful and versatile tools for biology (44–46). Further distance reduction to ∼10 to 30 nm and stable positioning could be achieved by introducing a fusion tag into the target gene and directly binding it with a nanobody (Fig. 9*B*) (44). Further improvements to the algorithm may also be able to address these issues.

A second set of limitations comes from the stochastic nature of SMLM. Fluorophores may blink many times, only once, or not at all (47). This phenomenon makes it difficult to distinguish nearby molecules of the same type. We employed an aggressive grouping algorithm to address this issue, but the tradeoff is that true separate molecules may be missed. We labeled our own secondary antibodies to control the dye:antibody ratio at ∼1:1 to limit multiple blinking, but the labeling creates a distribution, and some antibodies will still have multiple fluorophores. Antibodies engineered to have consistent labeling stoichiometry would be an improvement. A trade-off to limiting the dye:antibody ratio is that many of the secondary antibodies will have no fluorophore, reducing labeling efficiency. SMLM techniques generally have shown a

labeling efficiency of at most 60% (26). Improvements to labeling efficiency will enable rare binding interactions to be more readily detected by our method.

A third challenge for this algorithm comes from drift. Autocorrelation drift correction is standard, but it is optimal for defined structures that can be aligned from repeated blinks that occur throughout the acquisition. Singular soluble proteins, which blink only within a small window, pose a challenge for this correction method, and too few blinks overall can prevent the automatic correction from working despite apparent drift by eye. Further, this correction method cannot remove high-frequency variation in position through vibration within the microscope. Fluorescent beads may be used as a fiducial marker at the coverglass surface, but a solution is needed that would work throughout the cell. A sparsely labeled ubiquitous cellular structure, like tubulin, could serve this purpose with an appropriately engineered label. Eliminating drift effects would allow this algorithm to use smaller radii, increasing its sensitivity.

Despite these challenges, our technique provides a significant advance over existing methods in providing single-molecule-resolution information on protein and RNA associations inside the native cellular context. Desire for an SMLM
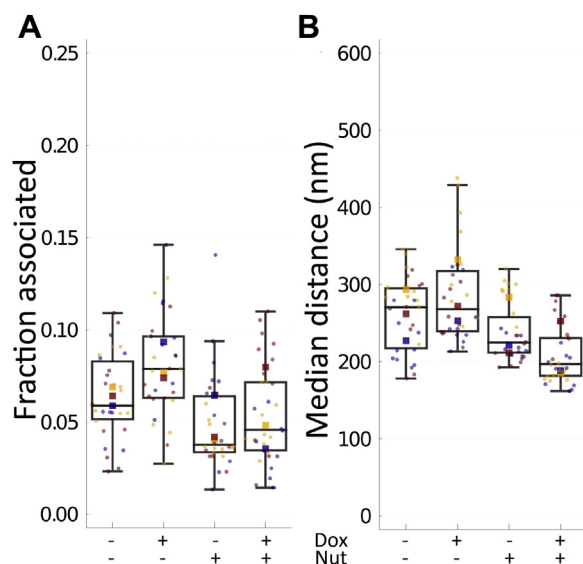
A

B

Figure 8. Neither nutlin-3a nor MEG3 significantly affected Mdm2–p53 binding. *MEG3* was induced by treatment of U2OS-MEG3 cells for 20 h with or without 1 μg/ml doxycycline and/or 10 μM nutlin-3a. Cells were then fixed and stained for 2-color dSTORM of p53 and Mdm2. For each condition, single molecule localizations were collected from 10 randomly chosen cells in three separate experiments. *A*, fraction of pairs associated, as defined by a probability of chance association <0.1 (*i.e.*, correction for local density) and distance <200 nm (upper limit for binding distance, accounting for error). *B*, median distance between pairs for each cell (nm). *Boxes* indicate median ± upper and lower quartile; *whiskers* indicate the range excluding outliers. Data points are colored by replicate. Means for each replicate are indicated by same-colored squares. * indicates $p < 0.05$ by ANOVA. dSTORM, direct stochastic optical reconstruction microscopy.

technique using a nearest neighbor approach has been discussed recently (26). Proximity ligation assays are also a comparable technique. In that technique, adjacent oligonucleotide-labeled antibodies are *in situ* amplified by rolling circle amplification and labeled with a fluorescent oligonucleotide probe (48). The strength of a PLA is that associated molecules are specifically identified in a cell, to the
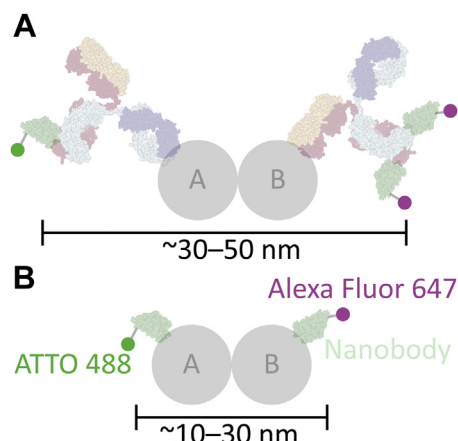
A

B

Figure 9. Nanobodies reduce distance between fluorophores for bound pairs. *A*, nanobodies (*pale green*) can be used in the place of secondary antibodies, reducing the distance to ∼30 to 50 nm. *B*, nanobodies may also be used to bind directly to a target of interest, either native or *via* a small peptide fusion tag, reducing the distance to ∼10 to 30 nm. Antibody and nanobody graphics were created using NGL Viewer (56) from RCSB PDB 1IGT and 5IVO, respectively.

exclusion of all nonassociated members, allowing a clear count of interactions. However, information on the total number of molecules is lost, and the resolution is limited. In contrast, SMLM enables the associations to be placed in the context of their whole cellular complement and can distinguish interactions between molecules located closer than the diffraction limit. Conceivably, one could develop a correlative SMLM-PLA approach to combine their strengths.

Previously, we found that MEG3 induces p53 stabilization and stimulates p53-dependent transcription activation (16). In this study, we demonstrated that MEG3 lncRNA interacts with p53 inside the cell and can be detected with a novel analytical method using dSTORM. We also demonstrated that the p53–Mdm2 interaction may not be significantly disrupted by MEG3 in cells. Taken together, these data suggest that an alternative mechanism leads to p53 activation. Finally, we believe our association analysis provides a powerful new tool to assess macromolecular interactions in a native cellular context, with future extensions to 3-dimensional data and multiprotein complexes.

Experimental procedures

Cell lines, media, and growth conditions

The U2OS osteosarcoma cells (ATCC HTB-96) were maintained in Dulbecco's modified Eagle's medium (Gibco 11995065) supplemented with 10% heat-inactivated FBS (Gibco A3060502), glutamine (2 mM), penicillin (100 U/ml), and streptomycin (0.1 mg/ml) (Gibco 10378016) at 37 °C and 10% CO_2. Doxycycline (Dox; 1 μg/ml) was added to media for at least 20 h to induce expression of the transfected tetracycline-inducible *MEG3*. Nutlin-3a (Nut; 10 μM) was added to media for at least 24 h to inhibit Mdm2-mediated degradation of p53. For microscopy, 3 to 5 × 10^4 cells were seeded into each well of a chambered 8-well 1.5H coverglass (Ibidi 80,827) and allowed to adhere overnight before further manipulation. Cells were tested for *mycoplasma* contamination every 3 months. U2OS-MEG3 cells were regularly authenticated by qRT-PCR and/or FISH for induction of MEG3 by doxycycline.

Plasmid construction and transfection

A modified Tet-On expression system was used to express MEG3, consisting of pBiTetO-MEG3-GFPLoxP and pCMV-rtTA3-IRESpuro. pBiTetO was constructed by replacing the CMV promoter in expression vector pCI with a tetracycline-responsive bi-directional promoter, BiTetO, which was synthesized to contain seven modified TetO elements flanked by two minimal CMV promoter sequences based on pTet-T2 sequences (GenScript) (49). To facilitate selection of clones, a GFP cDNA with the coding region flanked by two LoxP sites was cloned into pBiTetO to generate pBiTetO-GFPLoxP. The *MEG3* cDNA in pCI-MEG3 (16) was modified by replacing AATAAA and its downstream poly(A) tail with a genomic DNA fragment containing the *MEG3* gene polyadenylation signal. The resultant *MEG3* cDNA was then cloned into pBiTetO-GFPLoxP to generate pBiTetO-MEG3-GFPLoxP. To construct pCMV-rtTA3-IRESpuro, a modified tetracycline

responsive transactivator (rtTA3) was synthesized with changes in three amino acids including F67S, F86Y, and A209T (16, 50) and inserted into pIRESpuro3 (Clontech Laboratories). Plasmids were verified by sequencing.

For stable transfection, U2OS cells were seeded into 6-well cell culture plates and transfected with pBiTetO-MEG3-GFPLoxP and pCMV-rtTA3-IRESpuro at a ratio of 3 to 1 using Mirus TransIT-LT1 according to the manufacturer's instructions. Forty-eight hours after transfection, cells were re-seeded in P100 dishes with limited dilution. Approximately 10 days after treatment with puromycin (2 μg/ml), drug-resistant colonies were isolated using cloning rings. Cells from individual clones were treated with or without doxycycline (1 μg/ml) for 24 h. GFP expression was evaluated under a fluorescence microscope. Cells expressing GFP in Dox-treated wells were further examined for MEG3 expression by qRT-PCR. Two sets of primers were used to detect MEG3. The first set detected a fragment near the 5′ end of the MEG3 cDNA: 5′-ATTAAGCCCTGACCTTTGCTATGC-3′ (forward) and 5′-ATAAGGGTGATGACAGAGTCAGTCG-3′ (reverse); the second set detected the 3′ end of the MEG3: 5′-CTTCAGTGTCTGCATGTGGGAAG-3′ (forward) and 5′-TGCTTTGGAACCGCATCACAG-3′ (reverse). The GAPDH gene was used as an internal reference. The primers for detection of GAPDH were: 5′-GATGACATCAAGAAGGTGGTG AAGC-3′ (forward) and 5′-CGTTGTCATACCAGGAAA TGAGCTTG-3′ (reverse). Cell clones with suitable MEG3 induction were treated with adenoviruses expressing Cre (Ad-Cre) to remove the floxed GFP. Up to three rounds of virus treatments were needed to completely remove GFP. The removal of GFP was confirmed by qRT-PCR with primer set: 5′-CCA-CAACGTCTATATCATGGCCG-3′ (forward) and 5′-GTGCTCAGGTAGTGGTTGTCG-3′ (reverse). A total of four clones containing inducible MEG3 were finally obtained and designated as U2OS-MEG3.

Direct stochastic optical reconstruction microscopy

Fixation

Cells were grown between 30 and 90% confluence in chambered coverglass. Cells were rinsed with prewarmed Dulbecco's phosphate-buffered saline with calcium and magnesium (DPBS; Corning) twice using near-simultaneous aspiration and injection of liquid to avoid dehydration. Prewarmed fixation buffer [4% (v/v) paraformaldehyde (Electron Microscopy Sciences), 0.1% (v/v) glutaraldehyde (Electron Microscopy Sciences)] was added and incubated in the dark for 15 min. Fixed cells were rinsed with DPBS. Remaining fixative was quenched with 1% (w/v) sodium borohydride (Sigma-Aldrich) for 7 min (0.1% is typical, but we have observed better suppression of autofluorescence at 1%.) Cells were further quenched and washed with 50 mM glycine (Bio-Rad) in DPBS (DPBS-G) three times for 10 min each. Fixed cells were stored for up to a week in DPBS at 4 °C.

Immunofluorescence

Cells were permeabilized with 0.2% Triton X-100 (t-octyl-phenoxypolyethoxyethanol, Sigma-Aldrich) in DPBS for 10 min and rinsed with DPBS. Cells were blocked with 5% normal donkey serum (EMD Millipore)/0.02% (v/v) Triton X-100 in DPBS for 4 h at room temperature or overnight at 4 °C. Primary antibodies [rabbit anti-p53 (7F5) (Cell Signaling 2527S, Lot 8), mouse anti-Mdm2 (2A10) (Abcam ab16895, Lot GR324625−5)] were applied at 1:1000 and 1:200 dilutions, respectively, in blocking buffer and incubated overnight at 4 °C. Cells were washed with DPBS six times for 5 min each. Secondary antibodies [donkey anti-rabbit IgG (Jackson ImmunoResearch) and donkey anti-mouse IgG (Jackson ImmunoResearch)] were labeled as previously described with ATTO 488 (ThermoFisher Scientific) or Alexa Fluor 647 (ThermoFisher Scientific) for a dye ratio of ∼1:1 (51). Secondary antibodies were added at 3 μg/ml each in blocking buffer and incubated for 2 h at room temperature in the dark. All subsequent steps were performed in the dark. Cells were washed with DPBS six times for 5 min each. Antibody stacks were crosslinked by 4% (v/v) paraformaldehyde in DPBS for 15 min. Remaining fixative was quenched and washed with DPBS-G twice for 5 min each, followed by DPBS twice for 5 min each. Stained cells were stored at 4 °C for up to 2 weeks before imaging.

Combined immunofluorescence and fluorescence in situ hybridization

All buffers are RNase-free. Cells were permeabilized with 0.2% Triton X-100 in RNase-free PBS (Corning) for 10 min and rinsed with PBS. No blocking was performed to avoid introducing RNase activity. Primary antibody (rabbit anti-p53, see above) were applied at 1:1000 or 1:200 dilutions, respectively, in PBS and incubated overnight at 4 °C. Cells were washed with PBS six times for 5 min each. FISH was performed using buffers and ∼20-mer tiled probe sets from Stellaris, according to manufacturer's protocol. In brief, cells were washed with Wash Buffer A, 2 times for 3 min. MEG3-Quasar 670 (Stellaris, custom order) or GAPDH-Quasar 570 (Stellaris SMF-2026−1) probe mixture was mixed 1:1000 in hybridization buffer, and 100 μl was added per well. Steps from this point forward were conducted in the dark. The chambered coverglass was placed in a prewarmed humidified chamber (large culture dish with damp paper towels) and incubated at 37 °C for 16 h. Cells were washed two times for 15 min each with warm wash buffer A in the humidified chamber. Secondary antibodies (donkey anti-rabbit conjugated with ATTO 488, see above) were added at 3 μg/ml each in wash buffer A and incubated for 1 h at 37 °C in the humidified chamber. Cells were washed two times for 2 min each with wash buffer B, then two times for 5 min each with PBS.

Imaging

Imaging buffer containing 10 mM cysteamine (2-mercaptoethylamine; Sigma-Aldrich), 3 U/ml pyranose oxidase from *Coriolus* sp. (Sigma P4234), and 90 U/ml catalase was freshly prepared in STORM buffer. Cysteamine stock solution was previously titrated to pH 8 and aliquots frozen. Precipitate in pyranose oxidase/catalase 100x enzyme stock

solution was cleared by centrifugation at over 14,000×*g* before use. The STORM buffer was composed of 10% (w/v) glucose, 10 mM sodium chloride, and 50 mM Tris hydrochloride (pH 8.0). We found the pyranose oxidase buffer (first described in (52)) to be superior to the standard glucose oxidase buffer. This buffer allowed longer imaging times due to minimal pH change, and the enzyme stock lasted several months at 4 °C with no observable decline in imaging quality. Cysteamine (10 mM) was selected for superior imaging characteristics with different dyes (53). PBS was replaced with the imaging buffer, and the slide was mounted on the stage with type F immersion oil (refractive index = 1.515) on a Nikon Ti2 Eclipse inverted microscope. The microscope was equipped with a 100× 1.49 NA APO-TIRF objective with automatic correction collar and a Nikon NSTORM system including 405 nm (20 mW), 488 nm (70 mW), 561 nm (70 mW), and 647 nm (125 mW) lasers, a quadband excitation-emission filter, and a Hamamatsu ORCA Flash4.0 V2 S-CMOS camera. Nikon Elements 5.02 was used for image acquisition. A 10 × 10 tiled (with 15% overlap) widefield fluorescence image (∼790 × 790 μm^2) was obtained with 1 s exposure using GFPHQ, TexasRedHYQ, or Cy5HYQ filter cubes, from which random individual cells were selected for dSTORM imaging. At least 11,000, 256 x 256 pixel (160 nm/pixel) frames were collected with 10 ms exposure time at 100% laser power with lasers in highly inclined and laminated optical sheet configuration (54). Each channel was collected sequentially from longest wavelength to shortest.

Data analysis

Localizations were identified from STORM image stacks using Nikon Elements 5.02 (NSTORM 4.0), with a peak height threshold of 250. Localization lists were exported as tab-delimited text files.

Localization data were processed with custom code written in the freely available Julia scientific computing language (v1.6) (55). Localizations identified in the first 100 frames, while fluorophores are being placed into the "off" state, were excluded. Localizations identified in the last 10 frames were also excluded because of artifacts caused by the change in optical configuration. For each image, a grouping algorithm (Algorithm 1; Fig. S9) was applied to each channel to combine repeated blinking from single fluorophores and localizations that may be associated (*e.g.*, another fluorophore on same secondary antibody, another secondary antibody on the same primary antibody, another primary antibody on a multimer). The first stage of the grouping algorithm iteratively identified local density maxima by searching a 34.2 nm radius and within a temporal window of 500 frames (5.0 s) of each localization for the localizations with the most neighbors, combining those localizations within the radius of the maxima and repeating until all localizations were assigned to a group. The 34.2 nm radius limit was derived from a simulation of the possible orientation and positions of fluorophores in an antibody stack to account for possible motion of the antibody stack and multiple fluorophores on the stack. The temporal window was applied to account for longer-scale on/off cycles of the

fluorophores, as first described for PALM data (47), and was chosen semi-empirically by testing a range of values and selecting the smallest value that merged the most localizations (*i.e.*, where the slope starts to decrease before the plateau) (Fig. 10*A*) and where the merge results appeared suitable (*e.g.*, few temporally separated clusters of localizations were merged).

In the second stage, grouped localizations were merged if they were found within 200 nm of each other by a similar local density maxima search algorithm to further reduce redundancy from autocorrelated localizations. The products of this grouping algorithm were termed "molecules." The position of the resulting molecule was the mean of its component localizations' positions, and its linear localization accuracy was the mean of the accuracy for its component localizations divided by the square root of the number of component localizations.

The molecules were paired between channels by an exclusive cross-nearest neighbor algorithm (*i.e.*, closest pair found and then removed, next closest pair found and then removed…; Algorithm 3) to obtain a distance distribution between the two sets of molecules. Two analytical approaches were applied, simple and sophisticated. First, the median paired distance was calculated for each cell. Second, a novel approach was developed to control for local density, based on a similar approach applied to single-molecule conventional fluorescence microscopy (29) but with significant modifications to address the different characteristics of SMLM data. Random permutations (10,000) of the molecules in the local (800 nm radius) neighborhood around each potential binding pair were generated, and the closest pairwise distance in each permutation was calculated to create a Monte Carlo estimation of the distribution of distances due to local density (Algorithm 4). The local neighborhood radius of 800 nm was semi-empirically chosen based on testing multiple window sizes with the algorithm and choosing the value that provided a balance of sensitivity (smaller value) and robustness (less inter-sample change as parameter changes) (Fig. 10*B*). The fraction of permutations with a closest distance less than the observed distance was the percentile rank score, indicating the probability of chance association given the local density of both molecule types. Finally, the fraction of pairs within the maximum binding distance (200 nm) and with a probability of chance association of less than 0.1 was calculated for each cell. The maximum binding distance was chosen based on knowledge of the size of the target molecules (up to 20 nm across) and the size of the antibody stacks (up to 70 nm), with allowance for error.

Data are shown as mean ± standard deviation. Data were tested for significance by ANOVA with replicates as a repeated measure, as we observed correlation of values by replicate, with α = 0.05, using the SimpleANOVA.jl (v0.8.0) Julia package created by the authors. Generalized ω^2 effect size was interpreted as small (∼0.01), medium (∼0.06), and large (∼0.14). Data were checked for extreme outliers, heteroscedasticity, and normality of residuals and were determined to be reasonable. Single outlying datapoints with a z-score $\gtrsim 2.25$ in each sample were Windsorized. Plots were generated with StatsPlots.jl (v0.14.0) and assembled with Adobe Illustrator (24.0).
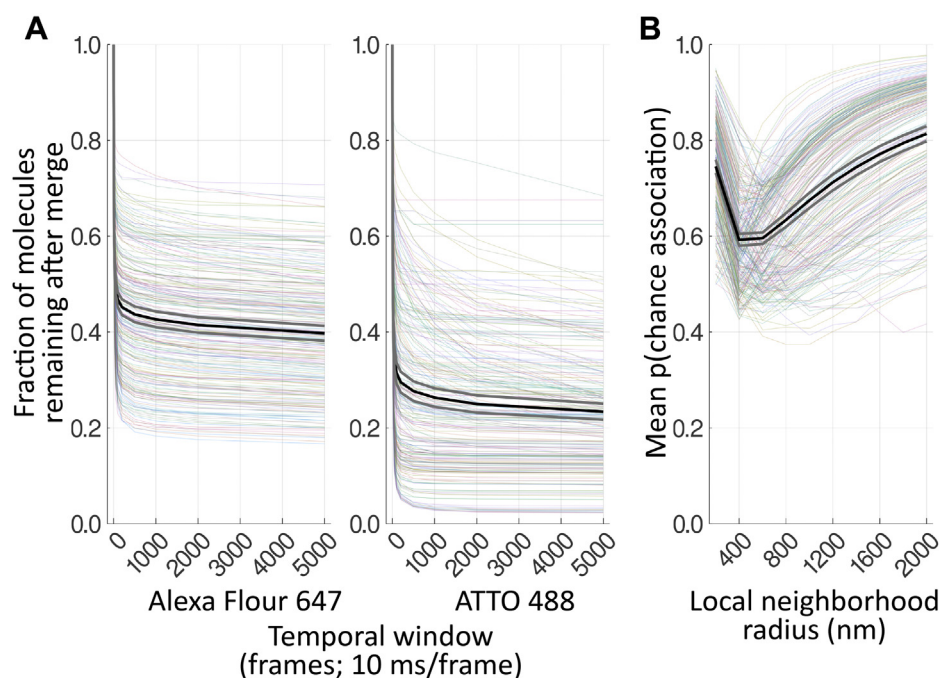
Figure 10. Analysis of algorithm parameters. All cells were repeatedly analyzed with the algorithm during development to characterize the effect of parameter choice on outcome. *A*, fraction of molecules remaining after grouping, normalized to the number of molecules with window size 1, as a function of temporal window size (frames, at 10 ms/frame), for Alexa Fluor 647 and ATTO 488. *B*, mean probability of chance association [p(chance association)] as a function of local neighborhood radius (nm). Each faded colored line is from a single cell. *Black line* shows the mean, *gray lines* indicate ±95% confidence interval.

Code availability

All the code generated specifically for this manuscript is written in the Julia language and available in the repository at https://doi.org/10.5281/zenodo.4542449. Supporting packages can be obtained within Julia from its public package registry.

Data availability

Raw STORM data files are stored on a local server. STORM localization list text files are available in the repository at https://doi.org/10.5281/zenodo.4542454.

References

1. Zhang, X., Zhou, Y., Mehta, K. R., Danila, D. C., Scolavino, S., Johnson, S. R., and Klibanski, A. (2003) A pituitary-derived MEG3 isoform functions as a growth suppressor in tumor cells. *J. Clin. Endocrinol. Metab.* **88**, 5119–5126
2. Naoki, M., Hirotaka, W., Shigeharu, W., Toshihiko, S., Masashi, N., Kohzoh, A., Takashi, K., Azim, S. M., Tomoko, K. I., and Fumitoshi, I. (2000) Identification of an imprinted gene, *Meg3/Gtl2* and its human homologue *MEG3*, first mapped on mouse distal chromosome 12 and human chromosome 14q. *Genes Cells* **5**, 211–220
3. Li, R., Fang, L., Pu, Q., Bu, H., Zhu, P., Chen, Z., Yu, M., Li, X., Weiland, T., Bansal, A., Ye, S. Q., Wei, Y., Jiang, J., and Wu, M. (2018) MEG3-4 is a miRNA decoy that regulates IL-1β abundance to initiate and then limit inflammation to prevent sepsis during lung infection. *Sci. Signal* **11**, eaao2387

4. Mondal, T., Subhash, S., Vaid, R., Enroth, S., Uday, S., Reinius, B., Mitra, S., Mohammed, A., James, A. R., Hoberg, E., Moustakas, A., Gyllensten, U., Jones, S. J., Gustafsson, C. M., Sims, A. H., *et al*. (2015) MEG3 long noncoding RNA regulates the TGF-beta pathway genes through formation of RNA-DNA triplex structures. *Nat. Commun.* **6**, 7743

5. Cheunsuchon, P., Zhou, Y., Zhang, X., Lee, H., Chen, W., Nakayama, Y., Rice, K. A., Tessa Hedley-Whyte, E., Swearingen, B., and Klibanski, A. (2011) Silencing of the imprinted *DLK1-MEG3* locus in human clinically nonfunctioning pituitary adenomas. *Am. J. Pathol.* **179**, 2120–2130

6. Gejman, R., Batista, D. L., Zhong, Y., Zhou, Y., Zhang, X., Swearingen, B., Stratakis, C. A., Hedley-Whyte, E. T., and Klibanski, A. D. (2008) Selective loss of MEG3 expression and intergenic differentially methylated region hypermethylation in the MEG3/DLK1 locus in human clinically nonfunctioning pituitary adenomas. *J. Clin. Endocrinol. Metab.* **93**, 4119–4125

7. Zhao, J., Dahle, D., Zhou, Y., Zhang, X., and Klibanski, A. D. (2005) Hypermethylation of the promoter region is associated with the loss of MEG3 gene expression in human pituitary tumors. *J. Clin. Endocrinol. Metab.* **90**, 2179–2186

8. Zhang, X., Gejman, R., Mahta, A., Zhong, Y., Rice, K. A., Zhou, Y., Cheunsuchon, P., Louis, D. N., and Klibanski, A. D. (2010) Maternally expressed gene 3, an imprinted noncoding RNA gene, is associated with meningioma pathogenesis and progression. *Cancer Res.* **70**, 2350–2358

9. Sheng, X., Li, J., Yang, L., Chen, Z., Zhao, Q., Tan, L., Zhou, Y., and Li, J. D. (2014) Promoter hypermethylation influences the suppressive role of maternally expressed 3, a long non-coding RNA, in the development of epithelial ovarian cancer. *Oncol. Rep.* **32**, 277–285

10. Jia, L. F., Wei, S. B., Gan, Y. H., Guo, Y., Gong, K., Mitchelson, K., Cheng, J., and Yu, G. Y. (2014) Expression, regulation and roles of miR-26a and MEG3 in tongue squamous cell carcinoma. *Int. J. Cancer* **135**, 2282–2293

11. Lu, K. H., Li, W., Liu, X. H., Sun, M., Zhang, M. L., Wu, W. Q., Xie, W. P., and Hou, Y. D. (2013) Long non-coding RNA MEG3 inhibits NSCLC cells proliferation and induces apoptosis by affecting p53 expression. *BMC Cancer* **13**, 461

12. Qu, C., Jiang, T., Li, Y., Wang, X., Cao, H., Xu, H., Qu, J., and Chen, J. G. (2013) Gene expression and IG-DMR hypomethylation of maternally expressed gene 3 in developing corticospinal neurons. *Gene Expr. Patterns* **13**, 51–56

13. Sun, M., Xia, R., Jin, F., Xu, T., Liu, Z., De, W., and Liu, X. D. (2014) Downregulated long noncoding RNA MEG3 is associated with poor prognosis and promotes cell proliferation in gastric cancer. *Tumour Biol.* **35**, 1065–1073

14. Huang, L., Yan, Z., Liao, X., Li, Y., Yang, J., Wang, Z. G., Zuo, Y., Kawai, H., Shadfan, M., Ganapathy, S., and Yuan, Z. M. (2011) The p53 inhibitors MDM2/MDMX complex is required for control of p53 activity *in vivo*. *Proc. Natl. Acad. Sci. U. S. A.* **108**, 12001–12006

15. Linares, L. K., Hengstermann, A., Ciechanover, A., Muller, S., and Scheffner, M. (2003) HdmX stimulates Hdm2-mediated ubiquitination and degradation of p53. *Proc. Natl. Acad. Sci. U. S. A.* **100**, 12009–12014

16. Zhou, Y., Zhong, Y., Wang, Y., Zhang, X., Batista, D. L., Gejman, R., Ansell, P. J., Zhao, J., Weng, C., and Klibanski, A. D. (2007) Activation of p53 by MEG3 non-coding RNA. *J. Biol. Chem.* **282**, 24731–24742

17. Ryan, K. M., Phillips, A. C., and Vousden, K. H. (2001) Regulation and function of the p53 tumor suppressor protein. *Curr. Opin. Cell Biol.* **13**, 332–337

18. Perry, M. E. (2010) The regulation of the p53-mediated stress response by MDM2 and MDM4. *Cold Spring Harb Perspect. Biol.* **2**, a000968

19. Toledo, F., and Wahl, G. M. (2006) Regulating the p53 pathway: In vitro hypotheses, *in vivo* veritas. *Nat. Rev. Cancer* **6**, 909–923

20. Gu, J., Kawai, H., Nie, L., Kitao, H., Wiederschain, D., Jochemsen, A. G., Parant, J., Lozano, G., and Yuan, Z. M. (2002) Mutual dependence of MDM2 and MDMX in their functional inactivation of p53. *J. Biol. Chem.* **277**, 19251–19254

21. Bauer, N. C., Doetsch, P. W., and Corbett, A. H. (2015) Mechanisms regulating protein localization. *Traffic* **16**, 1039–1061

22. Zheng, H., You, H., Zhou, X. Z., Murray, S. A., Uchida, T., Wulf, G., Gu, L., Tang, X., Lu, K. P., and Xiao, Z. X. (2002) The prolyl isomerase Pin1 is a regulator of p53 in genotoxic response. *Nature* **419**, 849–853

23. Zacchi, P., Gostissa, M., Uchida, T., Salvagno, C., Avolio, F., Volinia, S., Ronai, Z., Blandino, G., Schneider, C., and Del Sal, G. (2002) The prolyl isomerase Pin1 reveals a mechanism to control p53 functions after genotoxic insults. *Nature* **419**, 853–857

24. Zhu, J., Liu, S., Ye, F., Shen, Y., Tie, Y., Zhu, J., Wei, L., Jin, Y., Fu, H., Wu, Y., and Zheng, X. D. (2015) Long noncoding RNA MEG3 interacts with p53 protein and regulates partial p53 target genes in hepatoma cells. *PLoS One* **10**, e0139790

25. Yan, H., Yuan, J., Gao, L., Rao, J., and Hu, J. (2016) Long noncoding RNA MEG3 activation of p53 mediates ischemic neuronal death in stroke. *Neuroscience* **337**, 191–199

26. Feher, K., Halstead, J. M., Goyette, J., and Gaus, K. (2019) Can single molecule localization microscopy detect nanoclusters in T cells? *Curr. Opin. Chem. Biol.* **51**, 130–137

27. Pageon, S. V., Nicovich, P. R., Mollazade, M., Tabarin, T., and Gaus, K. (2016) Clus-DoC: A combined cluster detection and colocalization analysis for single-molecule localization microscopy data. *Mol. Biol. Cell* **27**, 3627–3636

28. Levet, F., Julien, G., Galland, R., Butler, C., Beghin, A., Chazeau, A., Hoess, P., Ries, J., Giannone, G., and Sibarita, J. B. (2019) A tessellation-based colocalization analysis approach for single-molecule localization microscopy. *Nat. Commun.* **10**, 2379

29. Eliscovich, C., Shenoy, S. M., and Singer, R. H. (2017) Imaging mRNA and protein interactions within neurons. *Proc. Natl. Acad. Sci. U. S. A.* **114**, E1875–E1884

30. Chen, X., Liu, M., Tian, Y., Li, J., Qi, Y., Zhao, D., Wu, Z., Huang, M., Wong, C. C. L., Wang, H. W., Wang, J., Yang, H., and Xu, Y. (2018) Cryo-EM structure of human mTOR complex 2. *Cell Res.* **28**, 518–528

31. Riley, K. J., and Maher, L. J., 3rd. (2007) p53 RNA interactions: new clues in an old mystery. *RNA* **13**, 1825–1833

32. Zhao, J., Ohsumi, T. K., Kung, J. T., Ogawa, Y., Grau, D. J., Sarma, K., Song, J. J., Kingston, R. E., Borowsky, M., and Lee, J. T. (2010) Genome-wide identification of polycomb-associated RNAs by RIP-seq. *Mol. Cell* **40**, 939–953

33. Kaneko, S., Bonasio, R., Saldana-Meyer, R., Yoshida, T., Son, J., Nishino, K., Umezawa, A., and Reinberg, D. (2014) Interactions between JARID2 and noncoding RNAs regulate PRC2 recruitment to chromatin. *Mol. Cell* **53**, 290–300

34. Vassilev, L. T., Vu, B. T., Graves, B., Carvajal, D., Podlaski, F., Filipovic, Z., Kong, N., Kammlott, U., Lukacs, C., Klein, C., Fotouhi, N., and Liu, E. A. (2004) *In vivo* activation of the p53 pathway by small-molecule antagonists of MDM2. *Science* **303**, 844–848

35. Wawrzynow, B., Pettersson, S., Zylicz, A., Bramham, J., Worrall, E., Hupp, T. R., and Ball, K. L. (2009) A function for the RING finger domain in the allosteric control of MDM2 conformation and activity. *J. Biol. Chem.* **284**, 11517–11530

36. Landré, V., Revi, B., Mir, M. G., Verma, C., Hupp, T. R., Gilbert, N., and Ball, K. L. (2017) Regulation of transcriptional activators by DNA-binding domain ubiquitination. *Cell Death Differ* **24**, 903–916

37. Herce, H. D., Deng, W., Helma, J., Leonhardt, H., and Cardoso, M. C. (2013) Visualization and targeted disruption of protein interactions in living cells. *Nat. Commun.* **4**, 2660

38. Das, P. P., Hendrix, D. A., Apostolou, E., Buchner, A. H., Canver, M. C., Beyaz, S., Ljuboja, D., Kuintzle, R., Kim, W., Karnik, R., Shao, Z., Xie, H., Xu, J., De Los Angeles, A., Zhang, Y., *et al*. (2015) PRC2 is required to maintain expression of the maternal *Gtl2-Rian-Mirg* locus by preventing de novo DNA methylation in mouse embryonic stem cells. *Cell Rep.* **12**, 1456–1470

39. Uroda, T., Anastasakou, E., Rossi, A., Teulon, J. M., Pellequer, J. L., Annibale, P., Pessey, O., Inga, A., Chillon, I., and Marcia, M. (2019) Conserved pseudoknots in lncRNA MEG3 are essential for stimulation of the p53 pathway. *Mol. Cell* **75**, 982–995.e989

40. Savchenko, A., Yurchenko, M., Snopok, B., and Kashuba, E. (2008) Study on the spatial architecture of p53, MDM2, and p14ARF containing complexes. *Mol. Biotechnol.* **41**, 270

41. Li, L., Tao, Q., Jin, H., van Hasselt, A., Poon, F. F., Wang, X., Zeng, M.-S., Jia, W.-H., Zeng, Y.-X., Chan, A. T. C., and Cao, Y. (2010) The tumor zuppressor UCHL1 forms a complex with p53/MDM2/ARF to promote

p53 signaling and is frequently silenced in nasopharyngeal carcinoma. *Clin. Cancer Res.* **16**, 2949–2958

42. Sloan, K. E., Bohnsack, M. T., and Watkins, N. J. (2013) The 5S RNP couples p53 homeostasis to ribosome biogenesis and nucleolar stress. *Cell Rep.* **5**, 237–247

43. Saphire, E. O., Stanfield, R. L., Crispin, M. D., Parren, P. W., Rudd, P. M., Dwek, R. A., Burton, D. R., and Wilson, I. A. (2002) Contrasting IgG structures reveal extreme asymmetry and flexibility. *J. Mol. Biol.* **319**, 9–18

44. Sograte-Idrissi, S., Oleksiievets, N., Isbaner, S., Eggert-Martinez, M., Enderlein, J., Tsukanov, R., and Opazo, F. (2019) Nanobody detection of standard fluorescent proteins enables multi-target DNA-PAINT with high resolution and minimal displacement errors. *Cells* **8**, 48

45. Carrington, G., Tomlinson, D., and Peckham, M. (2019) Exploiting nanobodies and affimers for superresolution imaging in light microscopy. *Mol. Biol. Cell* **30**, 2737–2740

46. Ingram, J. R., Schmidt, F. I., and Ploegh, H. L. (2018) Exploiting nanobodies' Singular Traits. *Annu. Rev. Immunol.* **36**, 695–715

47. Annibale, P., Vanni, S., Scarselli, M., Rothlisberger, U., and Radenovic, A. (2011) Identification of clustering artifacts in photoactivated localization microscopy. *Nat. Methods* **8**, 527

48. Young, R. M. (2019) Proximity ligation assay. In: Küppers, R., ed. *Lymphoma: Methods and Protocols*, Springer New York, New York, NY: 363–370

49. Loew, R., Heinz, N., Hampf, M., Bujard, H., and Gossen, M. (2010) Improved Tet-responsive promoters with minimized background expression. *BMC Biotechnol.* **10**, 81

50. Das, A. T., Zhou, X., Vink, M., Klaver, B., Verhoef, K., Marzio, G., and Berkhout, B. (2004) Viral evolution as a tool to improve the tetracycline-regulated gene expression system. *J. Biol. Chem.* **279**, 18776–18782

51. Schmider, A. B., Vaught, M., Bauer, N. C., Elliott, H. L., Godin, M. D., Ellis, G. E., Nigrovic, P. A., and Soberman, R. J. (2019) The organization of leukotriene biosynthesis on the nuclear envelope revealed by single molecule localization microscopy and computational analyses. *PLoS One* **14**, e0211943

52. Swoboda, M., Henig, J., Cheng, H. M., Brugger, D., Haltrich, D., Plumere, N., and Schlierf, M. (2012) Enzymatic oxygen scavenging for photostability without pH drop in single-molecule experiments. *ACS Nano* **6**, 6364–6369

53. van de Linde, S., Loschberger, A., Klein, T., Heidbreder, M., Wolter, S., Heilemann, M., and Sauer, M. (2011) Direct stochastic optical reconstruction microscopy with standard fluorescent probes. *Nat. Protoc.* **6**, 991–1009

54. Tokunaga, M., Imamoto, N., and Sakata-Sogawa, K. (2008) Highly inclined thin illumination enables clear single-molecule imaging in cells. *Nat. Methods* **5**, 159–161

55. Bezanson, J., Edelman, A., Karpinski, S., and Shah, V. B. (2017) Julia: A fresh approach to numerical computing. *SIAM Rev.* **59**, 65–98

56. Rose, A. S., Bradley, A. R., Valasatava, Y., Duarte, J. M., Prlić, A., and Rose, P. W. (2018) NGL viewer: Web-based molecular graphics for large complexes. *Bioinformatics* **34**, 3755–3758